THE ASTROPHYSICAL JOURNAL, 595:842–857, 2003 October 1

NONLINEAR HYDROMAGNETIC WAVE SUPPORT OF A STRATIFIED MOLECULAR CLOUD

TAKAHIRO KUDOH AND SHANTANU BASU
Department of Physics and Astronomy, University of Western Ontario, London, ON N6A 3K7, Canada;
kudoh@astro.uwo.ca, basu@astro.uwo.ca
Received 2003 March 7; accepted 2003 June 13

ABSTRACT

We perform numerical simulations of nonlinear MHD waves in a gravitationally stratified molecular cloud that is bounded by a hot and tenuous external medium. We study the relation between the strength of the turbulence and various global properties of a molecular cloud, within a 1.5-dimensional approximation. Under the influence of a driving source of Alfvénic disturbances, the cloud is lifted up by the pressure of MHD waves and reaches a steady state characterized by oscillations about a new time-averaged equilibrium state. The nonlinear effect results in the generation of longitudinal motions and many shock waves; however, the wave kinetic energy remains predominantly in transverse, rather than longitudinal, motions. There is an approximate equipartition of energy between the transverse velocity and fluctuating magnetic field (as predicted by small-amplitude theory) in the region of the stratified cloud that contains most of the mass; however, this relation breaks down in the outer regions, particularly near the cloud surface, where the motions have a standing-wave character. This means that the Chandrasekhar-Fermi formula applied to molecular clouds must be significantly modified in such regions. Models of an ensemble of clouds show that for various strengths of the input energy, the velocity dispersion in the cloud $\sigma \propto Z^{0.5}$, where Z is a characteristic size of the cloud. Furthermore, σ is always comparable to the mean Alfvén velocity of the cloud, consistent with observational results.

Subject headings: ISM: clouds — ISM: magnetic fields — methods: numerical — MHD — turbulence — waves

On-line material: color figures

1. INTRODUCTION

Interstellar molecular clouds, the sites of current star formation in our Galaxy, have long been known to yield supersonic line widths of molecular spectral lines (e.g., see Zuckerman & Palmer 1974). Objects classified as molecular clouds span a large range of mean radii ($R \sim 1$–100 pc), masses ($M \sim 10^2$–$10^6\ M_\odot$), and mean number density ($n \sim 10^1$–10^3 cm^{-3}). In fact, these quantities are correlated with the one-dimensional velocity dispersion σ through the well-known line-width–size–density relations (e.g., Solomon et al. 1987):

$$\sigma = 0.72(R/\mathrm{pc})^{0.5}\ \mathrm{km\ s^{-1}}\ , \tag{1}$$

$$n = 2.3 \times 10^3 (R/\mathrm{pc})^{-1}\ \mathrm{cm^{-3}}\ . \tag{2}$$

Thus, the velocity dispersion is typically supersonic since the sound speed c_s is only ≈ 0.2 km s^{-1} for the typical molecular cloud temperature $T \approx 10$ K (e.g., Goldsmith & Langer 1978).

The largest clouds, of mass $M \gtrsim 10^4\ M_\odot$, often classified as giant molecular clouds (GMCs) are in fact complexes of smaller clouds, since the volume-averaged density may be lower than the excitation density of CO (e.g., Blitz & Williams 1999), and also lower than allowed from thermal stability arguments (Falgarone & Puget 1986). Hence, the basic building blocks of interstellar molecular clouds, which contain most of mass of molecular material, are the dark (or dwarf) molecular clouds, which have $R \sim 1$–10 pc, $M \sim 10^2$–$10^4\ M_\odot$, and $n \sim 10^2$–10^3 cm^{-3}. These clouds have velocity dispersion $\sigma \sim 1$–2 km s^{-1} and represent the class of objects that we are interested in modeling in this study. We also note that observed smaller scale ($R \sim 0.1$ pc) dense cores are a separate object class that are embedded within dark clouds and collectively contain only a small fraction of the total cloud mass.

While even dark clouds have masses that significantly exceed the thermal Jeans (1928) mass

$$M_J = \left(\frac{\pi k T}{mG}\right)^{3/2} \frac{1}{\rho^{1/2}} = 17 \left(\frac{T}{10\ \mathrm{K}}\right)^{3/2} \left(\frac{n}{10^3\ \mathrm{cm^{-3}}}\right)^{-1/2} M_\odot \tag{3}$$

(where we have used $\rho = mn$ and $m = 2.33 m_\mathrm{H}$, in which m_H is the mass of a hydrogen atom), the line-width–size–density relations do imply that molecular clouds are individually in an *approximate* virial balance between turbulent and gravitational energies. In this paper we equate the presence of nonthermal line widths with the presence of a random superposition of nonlinear (presumably hydromagnetic) waves and refer loosely to the latter as "turbulence." Within each cloud, the turbulence is expected to collectively exert a force (e.g., Chandrasekhar 1951) that resists the inward pull of gravity.

The origin and persistence of turbulent motions in molecular clouds remain an active area of investigation. It was long understood (see Mestel 1965; Goldreich & Kwan 1974) that supersonic hydrodynamic motions would decay rapidly through shocks, thereby creating a mystery of why the turbulence was commonly observed throughout the lifetime of molecular clouds. For GMCs, the lifetime is estimated to be a few times 10^7 yr (e.g., Blitz & Williams 1999), which is at least a few times longer than the crossing time $t_c \equiv 2R/\sigma$ of the complexes. The smaller dark molecular clouds may have even longer lifetimes $\sim 10^8$ yr (Shu, Adams, & Lizano 1987). Since slow- and fast-mode MHD waves are also compressive and can be highly dissipative, it was suggested by Arons & Max (1975) that the transverse Alfvén mode might be a long-lived

component, thereby preventing a rapid overall collapse of the clouds and explaining the observed persistence of the turbulence over their inferred lifetime. Mouschovias (1975) made the related suggestion that the long-lived component may be due to standing waves, i.e., normal mode oscillations, of magnetized clouds. Such global magnetogravitational motions cannot be studied with a simple plane wave analysis in an infinite uniform medium.

The MHD wave picture has been strengthened by the detection of large-scale magnetic fields within molecular clouds, through maps of polarized absorption and emission (e.g., Vrba, Strom, & Strom 1976; Goodman et al. 1990; Schleuning 1998; Matthews & Wilson 2002) and Zeeman measurements of the line-of-sight magnetic field strengths (Crutcher 1999 and references therein). The latter imply that the magnetic energy (like the turbulent energy) is comparable to the gravitational potential energy; equivalently, the mass-to-flux ratio is close to a critical value

$$\left(\frac{M}{\Phi}\right)_{\rm crit} = c_1\, G^{-1/2}\,. \tag{4}$$

In the above equation, the constant c_1 has been calculated to be in the range 0.13–0.17 on the basis of detailed two-dimensional equilibrium states (Mouschovias & Spitzer 1976; Tomisaka, Ikeuchi, & Nakamura 1988) and is equal to $1/(2\pi)$ in the case of a flattened one-dimensional layer (Nakano & Nakamura 1978). Collectively, the magnetic field measurements allow the possibility that clouds are supported lateral to the large-scale field B by its associated Lorentz force, while these magnetic field lines act as a carrier of Alfvénic disturbances with $\delta B \sim B$, explaining the observed spectral line widths and preventing the clouds from assuming a very flattened configuration,

The dynamical effect of propagating MHD waves using analytic or semianalytic means has been studied by several authors. Dewar (1970) developed a formalism for calculating the effect of small-amplitude hydromagnetic waves on a slowly varying background medium, using the WKB approach. Assuming ideal MHD and no dissipation of the waves, this leads to a steady state relation between wave pressure P_w and gas density ρ of the form $P_w \propto \rho^{1/2}$ (McKee & Zweibel 1995). Simplified calculations of the effect of small-amplitude MHD waves on a molecular cloud have been performed by Fatuzzo & Adams (1993) and Martin, Heyvaerts, & Priest (1997). Both satisfy the above scaling of P_w in the ideal MHD limit. In particular, the WKB model of Martin et al. (1997) yields a steady state density structure of an infinite one-dimensional cloud supported by short-wavelength Alfvén waves in the ideal MHD limit, and also when accounting for damping of linear waves by ion-neutral friction. In addition to ion-neutral friction, which damps even linear waves (Kulsrud & Pearce 1969), there are several nonlinear effects that will work to enhance dissipation. The second-order effect of a gradient in the magnetic pressure $\nabla \delta B^2/8\pi$ will in general lead to steepening of the waves followed by dissipation (Cohen & Kulsrud 1974). Zweibel & Josafatsson (1983) state the form of this dissipation rate, which can dominate the process of ion-neutral friction for nonlinear and/or long wavelength modes. There are also other known nonlinear avenues for wave dissipation, such as the conversion of a parallel-propagating Alfvén wave into an acoustic wave and another Alfvén wave traveling in the opposite direction (Sagdeev & Galeev 1969).

Recently, several studies have resulted in a solution of the full set of nonlinear equations of ideal MHD using finite difference approximations. Gammie & Ostriker (1996) performed a one-dimensional numerical simulation of MHD turbulence in a periodic domain. This has been followed up by several multidimensional simulations, also in a periodic domain (e.g., Stone, Ostriker, & Gammie 1998; Ostriker, Gammie, & Stone 1999; Mac Low et al. 1998; Mac Low 1999; Padoan & Nordlund 1999; Ostriker, Stone, & Gammie 2001). These models impose prescribed velocity fluctuations, at the initial time and sometimes also throughout the computed time, and investigate the dissipation rate of turbulence, as well as various properties of turbulent fluctuations. One of the important results of these papers is that the decay time of the MHD turbulence is comparable to the crossing time over the driving scale of the turbulence. The nonlinear coupling of the Alfvén to the fast- and slow-mode MHD waves is considered to be a significant source of the dissipation that reduces the lifetime of MHD turbulence relative to the ideal of pure Alfvénic turbulence. We note that periodic models represent only a local region of a much larger molecular cloud and maintain a fixed mean density. They cannot study global effects associated with the density stratification in a cloud or the existence of a cloud boundary.

In this paper we perform a different type of numerical simulation of MHD turbulence. We concentrate on one self-gravitating cloud and study the effect of the turbulence on the mechanical structure of the cloud. This corresponds to an extension of the model studied by Martin et al. (1997) into a fully nonlinear counterpart. As an initial condition, we use a hydrostatic equilibrium between thermal pressure and self-gravity in a cloud that is bounded by an external high-temperature medium. We input turbulent energy into the system continuously and see how the mechanical equilibrium changes. Similar numerical simulations have been performed to study the propagation of Alfvén waves in the solar chromosphere and corona (e.g., Hollweg, Jackson, & Galloway 1982; Mariska & Hollweg 1985; Hollweg 1992; Kudoh & Shibata 1999; Saito, Kudoh, & Shibata 2001). We extend this class of model to a self-gravitating cloud and study the relation between the strength of the turbulence and various global properties of a molecular cloud. This is the first of a series of papers on global models of MHD wave support in molecular clouds. In this paper we develop high-resolution one-dimensional models under the assumption of ideal MHD.

The paper is organized as follows. The numerical model we used for the simulation is summarized in § 2. The results of the simulation are described in § 3. We add some discussion of the results in § 4 and summarize the paper in § 5.

2. THE NUMERICAL MODEL

2.1. *Schematic View of Our Model*

Figure 1 shows a schematic picture of our model. We consider a molecular cloud that is threaded by a large-scale magnetic field and concentrate on a local region of the molecular cloud enclosed by the rectangle in the figure. We assume a driving force near the midplane of the cloud and follow the dynamical evolution of the vertical structure of the cloud.

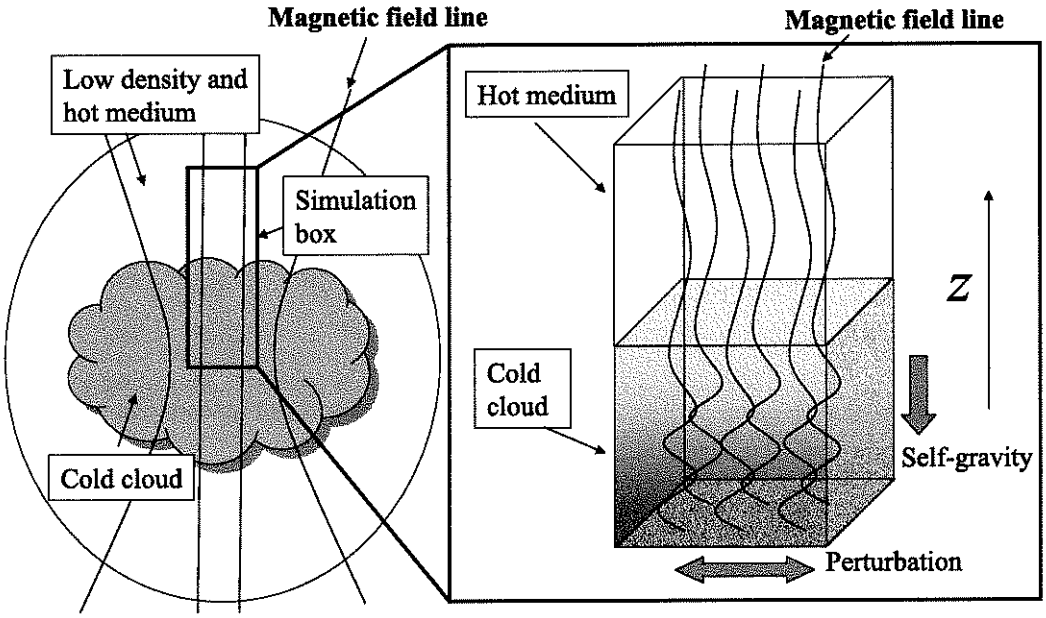

FIG. 1.—Schematic picture of our model. A molecular cloud that is threaded by a large-scale magnetic field is considered. A local region of the molecular cloud enclosed by the rectangle in the figure can represent the region that we are modeling in this paper. We input a driving force near the midplane of the cloud and follow the dynamical evolution of the vertical structure of the cloud.

2.2. *Assumptions*

For simplicity, we assume ideal MHD, 1.5 dimensions, and isothermality for each Lagrangian fluid element. The 1.5-dimensional approximation means that physical quantities depend on only one coordinate, but we evolve nonzero components of vectors in one additional direction. Isothermality for each Lagrangian fluid element means that the temperature does not change in time for each fluid element as it moves through Eulerian space, which is different from the assumption of a uniform time-independent temperature throughout the region. These assumptions appear in § 2.3 more concretely.

2.3. *Basic Equations*

We use local Cartesian coordinates (x, y, z) on the molecular cloud, where we set z to be the direction of the large-scale magnetic field. According to the symmetry of the 1.5-dimensional approximation, we set

$$\frac{\partial}{\partial x} = \frac{\partial}{\partial y} = 0 \,. \tag{5}$$

The above symmetry and the divergence-free condition on the magnetic field imply

$$B_z = \text{constant} \,, \tag{6}$$

where B_z is the z-component of the magnetic field that threads the molecular cloud. Moreover, from the assumption of linear polarization of the waves, we can set

$$v_x = B_x = 0 \tag{7}$$

without loss of generality, where v_x and B_x are the x-components of the velocity and magnetic field, respectively.

Therefore, the basic MHD equations that we use in this paper are as follows: mass conservation,

$$\frac{\partial \rho}{\partial t} + v_z \frac{\partial \rho}{\partial z} = -\rho \frac{\partial v_z}{\partial z} \,; \tag{8}$$

the z-component of the momentum equation,

$$\frac{\partial v_z}{\partial t} + v_z \frac{\partial v_z}{\partial z} = -\frac{1}{\rho}\frac{\partial P}{\partial z} - \frac{1}{4\pi\rho} B_y \frac{\partial B_y}{\partial z} + g_z \,; \tag{9}$$

the y-component of the momentum equation,

$$\frac{\partial v_y}{\partial t} + v_z \frac{\partial v_y}{\partial z} = \frac{1}{4\pi\rho} B_z \frac{\partial B_y}{\partial z} \,; \tag{10}$$

the equation of energy,

$$\frac{\partial T}{\partial t} + v_z \frac{\partial T}{\partial z} = -(\gamma - 1) T \frac{\partial v_z}{\partial z} \,; \tag{11}$$

the y-component of the induction equation,

$$\frac{\partial B_y}{\partial t} = \frac{\partial}{\partial z}(-v_z B_y + v_y B_z) \,; \tag{12}$$

the equation of state,

$$P = \rho \frac{kT}{m} = c_s^2 \rho \,, \tag{13}$$

where

$$c_s \equiv \sqrt{\frac{kT}{m}} \tag{14}$$

is the isothermal sound speed; and the Poisson equation,

$$\frac{\partial g_z}{\partial z} = -4\pi G \rho \,. \tag{15}$$

In these equations, t is the time, G is the gravitational constant, k is Boltzmann's constant, m is the mean molecular mass, γ is the specific heat ratio, ρ is the density, P is the pressure, T is the temperature, g_z is the z-component of the gravitational field, v_z is the z-component of velocity, v_y is the y-component of velocity, and B_y is the y-component of the magnetic field.

In equation (11), we assume $\gamma = 1$, so that the energy equation becomes

$$\frac{\partial T}{\partial t} + v_z \frac{\partial T}{\partial z} = 0 , \tag{16}$$

which quantifies the assumption of isothermality for each Lagrangian fluid element.

2.4. *Initial Conditions*

As an initial condition, we assume hydrostatic equilibrium of a self-gravitating one-dimensional cloud. The hydrostatic equilibrium is calculated from the equations

$$\frac{1}{\rho}\frac{dP}{dz} = g_z , \tag{17}$$

$$\frac{dg_z}{dz} = -4\pi G\rho , \tag{18}$$

$$P = \rho \frac{kT}{m} , \tag{19}$$

subject to the boundary conditions

$$g_z(z = 0) = 0 , \tag{20}$$

$$\rho(z = 0) = \rho_0 , \tag{21}$$

$$P(z = 0) = \rho_0 \frac{kT_0}{m} , \tag{22}$$

where ρ_0 and T_0 are the initial density and initial temperature at $z = 0$, respectively.

In order to solve the above equations, we need to assume an initial temperature distribution. If the temperature is uniform throughout the region, we have the following analytic solution ρ_S found by Spitzer (1942):

$$\rho_S(z) = \rho_0 \operatorname{sech}^2(z/H_0) , \tag{23}$$

where

$$H_0 = \frac{c_{s0}}{\sqrt{2\pi G\rho_0}} \tag{24}$$

is the scale height and

$$c_{s0} = \sqrt{\frac{kT_0}{m}} . \tag{25}$$

However, an isothermal molecular cloud is usually surrounded by warm or hot material, such as neutral hydrogen or ionized gas. Therefore, we assume the initial temperature distribution to be

$$T(z) = T_0 + \frac{1}{2}(T_c - T_0)\left[1 + \tanh\left(\frac{|z| - z_c}{z_d}\right)\right] , \tag{26}$$

where we take $T_c = 100T_0$, $z_c = 3H_0$, and $z_d = 0.2H_0$ throughout the paper. This distribution shows that the temperature is uniform and equal to T_0 in the region of $0 \le z < z_c = 3H_0$ and smoothly increases to another uniform value $T_c = 100T_0$ at $z \simeq z_c = 3H_0$. By using this temperature distribution, we can solve the ordinary differential equations (17)–(19) numerically. The numerical solution of these equations shows that the initial distribution of density is almost the same as Spitzer's solution in the region of $0 \le z < z_c$ (see Fig. 2).

We also assume the following initial conditions:

$$v_z(z) = v_y(z) = 0 , \tag{27}$$

$$B_y(z) = 0 , \tag{28}$$

$$B_z(z) = B_0 , \tag{29}$$

where B_0 is a constant. According to equation (6), B_z is spatially uniform and independent of time throughout the calculations.

2.5. *Driving Force*

We introduce a perturbation into the initially hydrostatic cloud by adding a driving force, $F(z, t)$, into the y-component of the momentum equation (10) as follows:

$$\rho\left(\frac{\partial v_y}{\partial t} + v_z \frac{\partial v_y}{\partial z}\right) = \frac{1}{4\pi} B_z \frac{\partial B_y}{\partial z} + F(z, t) , \tag{30}$$

where

$$F(z, t) = \begin{cases} \rho a_d \left(\dfrac{t}{10t_0}\right) \sin(2\pi\nu_0 t) \exp\left[-\left(\dfrac{z}{z_a}\right)^2\right] & (t < 10t_0) , \\ \rho a_d \sin(2\pi\nu_0 t) \exp\left[-\left(\dfrac{z}{z_a}\right)^2\right] & (10t_0 \le t \le 40t_0) , \\ 0 & (t > 40t_0) , \end{cases} \tag{31}$$

and

$$t_0 = \frac{H_0}{c_{s0}} . \tag{32}$$

Furthermore, a_d is the amplitude of the induced acceleration, ν_0 is the frequency of the driving force, and z_a represents the region in which we input the driving force. The equations show that we input the sinusoidal driving force near the midplane of the cloud, and we increase the maximum driving force linearly with time until $t = 10t_0$ and maintain it to be constant during $10t_0 \le t \le 40t_0$. After $t = 40t_0$, we terminate the driving force.

2.6. *Boundary Conditions*

We used a mirror-symmetric boundary condition at $z = 0$ and a free boundary at $z = z_{out}$, the outer boundary of the calculation. In order to remove the reflection of waves at the outer boundary, we set z_{out} to be a large value, i.e.,

$$z_{out} \simeq 2.6 \times 10^4 H_0 , \tag{33}$$

and use nonuniform grid spacing for large z (see § 2.8).

In addition to this, we set the gravitational field to be zero at large distances by introducing an artificial acceleration

(g_-) into equations (9) and (17), i.e.,

$$g_-(z) = -\frac{g_z(z)}{2}\left[1 + \tanh\left(\frac{z - z_g}{5H_0}\right)\right], \quad (34)$$

where we take $z_g = 100H_0$ in this paper. This force is zero until $z \simeq z_g = 100H_0$, but it becomes essentially equal to g_z with negative sign for $z > z_g = 100H_0$ and compensates the gravity there.

The above boundary conditions show that we have effectively two outer boundaries. The first one is $z_{\rm out}$, and the second one is z_g, which is the boundary for the gravitational field. In order to remove the reflection of waves at the outer boundary, it is useful to have a large $z_{\rm out}$. However, a very large $z_{\rm out}$ introduces numerical problems because the density decreases exponentially at large z, according to the stratification of a self-gravitating cloud. A very low density leads to a very large Alfvén speed, making simulations inefficient by forcing very small time steps for an explicit calculation. By setting the net gravitational field to be zero at large distances, we can avoid an extremely low density for large z and therefore take a large $z_{\rm out}$ in order to remove the reflection of Alfvén waves at the outer boundary. We also note that for any slab of finite extent, as opposed to the infinite slab implied by our one-dimensional model, the net gravitational field should indeed decrease at large distances, although not in the specific manner prescribed here.

Because of the added artificial acceleration, our effective numerical boundary is located at $z \simeq z_g = 100H_0$, and we cannot trust the results beyond this region. However, as we show later, all dynamical events we are interested in occur within $z < 50H_0$, where most of the mass and energy are concentrated. Hence, the effect of the artificial acceleration is negligible for the main results in this simulation.

2.7. *Numerical Parameters*

A natural set of fundamental units for this problem are c_{s0}, H_0, and ρ_0. These yield a time unit $t_0 = H_0/c_{s0}$. The initial magnetic field strength introduces one dimensionless free parameter, i.e.,

$$\beta_0 \equiv \frac{8\pi P_0}{B_0^2} = \frac{8\pi\rho_0 c_{s0}^2}{B_0^2}, \quad (35)$$

which is the initial ratio of gas to magnetic pressure at $z = 0$.

In this cloud, β_0 is related to the mass-to-flux ratio. For Spitzer's self-gravitating cloud, the mass-to-flux ratio normalized to the critical value is

$$\mu_{\rm S} \equiv 2\pi G^{1/2}\frac{\Sigma_{\rm S}}{B_0}, \quad (36)$$

where

$$\Sigma_{\rm S} = \int_{-\infty}^{\infty}\rho_{\rm S}\,dz = 2\rho_0 H_0 \quad (37)$$

is the column density of Spitzer's self-gravitating cloud. Therefore,

$$\beta_0 = \mu_{\rm S}^2. \quad (38)$$

The column density of the cloud we used in this paper is almost equal to that of Spitzer's cloud. If we define the column density of the cloud, Σ, as the integral of density within $-z_c < z < z_c$, then

$$\Sigma = \int_{-z_c}^{z_c}\rho(t=0)dz \simeq 0.988\Sigma_{\rm S}. \quad (39)$$

This means that we can use the value of $\mu_{\rm S}$ as an excellent approximation to the dimensionless mass-to-flux ratio of the model cloud.

Observations show that the dimensionless mass-to-flux ratios of molecular clouds are close to unity over a range of scales (Crutcher 1999; Shu et al. 1999). Hence, we take $\beta_0 = 1$ in the models presented in this paper.

The driving force introduces three more important free parameters: $\tilde{a}_d = a_d(H_0/c_{s0}^2)$, the dimensionless amplitude of the acceleration due to driving, $\tilde{\nu}_0 = \nu_0 t_0$, the dimensionless frequency of driving, and $\tilde{z}_a = z_a/H_0$, the dimensionless scale of the driving region. For simplicity, we take $\tilde{\nu}_0 = 1$ and $\tilde{z}_a = 0.1$ throughout this paper and adjust the strength of driving by varying $\tilde{a}_d$ from 10 to 50.

Dimensional values of all quantities can be found through a choice of T_0 and ρ_0, along with the values of the dimensionless free parameters. For example, if $T_0 = 10$ K and $n_0 = \rho_0/m = 10^4$ cm^{-3}, then $c_{s0} = 0.2$ km s^{-1}, $H_0 = 0.05$ pc, $N_{\rm S} = \Sigma_{\rm S}/m = 3 \times 10^{21}$ cm^{-2}, $t_0 = 2.5 \times 10^5$ yr, and $B_0 = 20$ μG if $\beta_0 = 1$.

2.8. *Numerical Technique*

In order to solve the equations numerically, we use the CIP method (Yabe & Aoki 1991) for equations (8)–(10), and (16), and the method of characteristics-constrained transport (MOCCT) (Stone & Norman 1992) for equation (12). The combination of the CIP and MOCCT methods is summarized in Kudoh, Matsumoto, & Shibata (1999). The CIP method is a useful method to solve advection equations such as equation (16) accurately and is also applicable to advection terms of equations (8)–(10).

Because of the mirror-symmetric boundary condition at $z = 0$, Poisson equation (15) can be simply integrated from the midplane of the cloud:

$$g_z(z) = -4\pi G\int_0^z\rho(z)dz. \quad (40)$$

We solve this equation by numerical integration.

In this simulation, we actually use variants of the original CIP method. We use a conservative-CIP method for the mass conservation equation (8), which was recently developed by Xiao et al. (2002). This scheme assures exact conservation of mass and less numerical oscillations. The original CIP method does not assure the exact conservation of mass, so that a systematic deviation during each time step can cause a problem for long time integrations; this is especially a problem if the Poisson equation, which utilizes the mass distribution, is being solved simultaneously. Hence, the conservative-CIP method significantly improves the accuracy of our solution. We also use the monotonic-CIP method (Xiao, Yabe, & Ito 1996) for the advection terms of equations (9), (10) and (16), and use the CCUP method (Yabe & Wang 1991) for the calculation of gas pressure, in order to get more numerically stable results. The recent developments of CIP related schemes are summarized in Yabe, Xiao, & Utsumi (2001).

We used a uniform grid size, $\Delta z_i = 0.02H_0$, from $z = 0$ to $z = 80H_0$, where Δz_i is the grid size of the ith grid point. For $80H_0 < z < 120H_0$, we gradually increase the grid size as $\Delta z_{i+1} = \min(1.05\Delta z_i, 0.2H_0)$, where min is a function that picks the minimum from the two values; hence, the maximum grid size in this region is $0.2H_0$. For $120H_0 < z < z_{\rm out}$, where the gravitational field is compensated by the artificial force, we further increase the grid size according to $\Delta z_{i+1} = 1.05\Delta z_i$. In this paper we used a total of 4310 grid points, most of which are concentrated in the region of the uniform grid, i.e., $z \leq 80H_0$.

3. RESULTS

3.1. *Typical Result*

In this subsection, we show the results of $\tilde{a}_d = 30$ as the typical case.

3.1.1. *Density Structure in the Cloud*

Figure 2 shows the density and temperature as a function of z. The dashed lines show the initial distributions, and the solid lines show the distribution at $t = 30t_0$.

The dotted line in the density shows the distribution of Spitzer's self-gravitating cloud with a uniform temperature T_0. The initial density deviates from Spitzer's solution around $z = z_c = 3H_0$ where the initial temperature increases

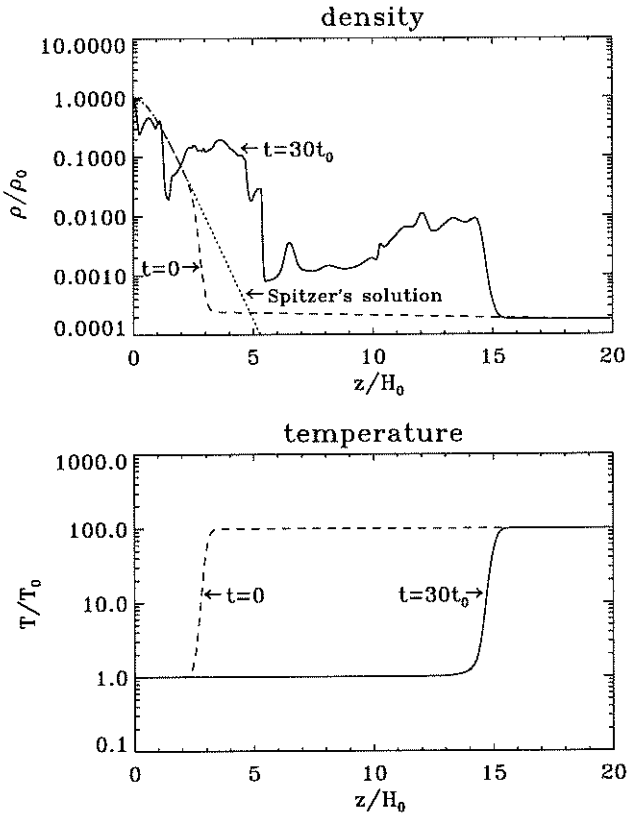

FIG. 2.—Density (*upper panel*) and temperature (*lower panel*) as a function of z. The dashed lines show the initial distributions and the solid lines show the distribution at $t = 30t_0$. The dotted line in the density plot shows the distribution of density in Spitzer's infinite self-gravitating equilibrium with a uniform temperature T_0.

up to $100T_0$. The density decreases rapidly around $z = z_c = 3H_0$ because of the pressure balance between low-temperature cloud and high-temperature external medium. For $z > z_c = 3H_0$, the scale height of the density is very large and the density decreases gradually.

The snapshot of density at $t = 30t_0$ shows that the density has a complicated structure including many shock fronts. This is caused by the driving force in equation (30). The driving force generates nonlinear Alfvén waves in the cloud that produce a magnetic pressure gradient. The magnetic pressure gradient and thermal pressure gradient usually push the cloud upward, but the self-gravity of the cloud always pulls it down. These up and down motions create the complicated structure in the cloud. On the other hand, the temperature shows a smooth structure. This is due to isothermality for each Lagrangian fluid element. Only the position of the temperature transition region changes in time.

Figure 3 shows the time evolution of the density. The density plots at various times are stacked with time increasing upward in uniform increments of $0.2t_0$. Because the driving force increases linearly with time up to $t = 10t_0$, the density changes gradually at first. After $t = 10t_0$, the density structure shows many shock waves propagating in the cloud and significant upward and downward motions of the outer portion of the cloud, including the transition region. After terminating the driving force at $t = 40t_0$, the shock waves are dissipated in the cloud and the transition region falls to around the initial position, although it is still oscillating.

Figure 4*a* shows the column density as a function of the time-averaged position of several Lagrangian fluid elements, which are equally spaced at time $t = 0$ with spacing $\Delta z = 0.1H_0$ starting at $z = 0.01H_0$. The time average is calculated between $t = 10t_0$ and $t = 40t_0$, while the driving force is input with constant amplitude. The dashed line shows the initial distribution.

The Lagrangian fluid elements have constant enclosed column density as a function of time. By using this property, we evaluate the location of Lagrangian fluid elements from the surface density. The difference between the initial distribution and that of the time average shows that the cloud is lifted up. Figure 4*b* shows the time average of the density for each element as a function of the time-averaged position of each element. These time averages were also calculated between $t = 10t_0$ and $t = 40t_0$. In contrast to the snapshot in Figure 2, the time-averaged density structure shows a smooth distribution. The dashed line shows the initial density distribution of the cloud. The scale height of the time-averaged distribution is about 3 times larger than the initial value.

3.1.2. *Velocities in the Cloud*

Figure 5*a* shows the time evolution of v_y at $z = 0$. Initially, it is oscillating about zero sinusoidally with the frequency of the driving force. However, as time goes on, the oscillation shows sharp structures, and it becomes nonsymmetric around the mean. The sharp structures are caused by nonlinear effects in the cloud such as shock waves. Moreover, the mean value shows a deviation from zero as time goes on. This implies that the net y-momentum of the cloud is not zero and the cloud has a mean motion in the y-direction as well as an oscillatory motion.

This mean motion is ultimately caused by the driving force. Prior to $t = 10t_0$, the driving force is not symmetric in

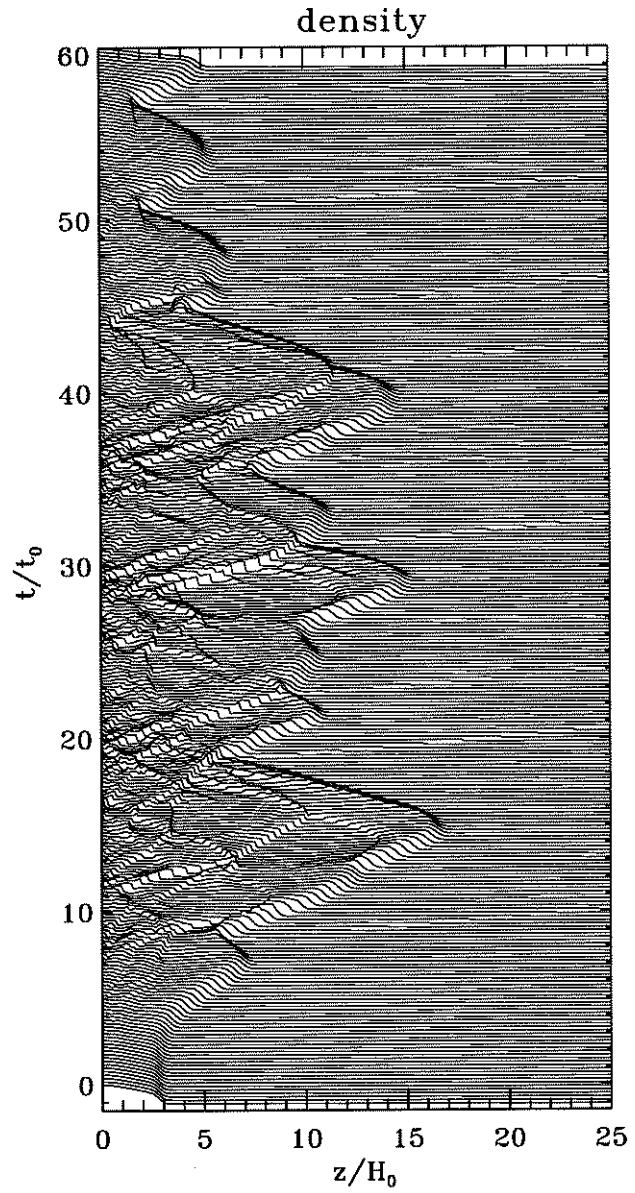

FIG. 3.—Time evolution of the density. The density plots at various times are stacked with time increasing upward in uniform increments of $0.2t_0$.

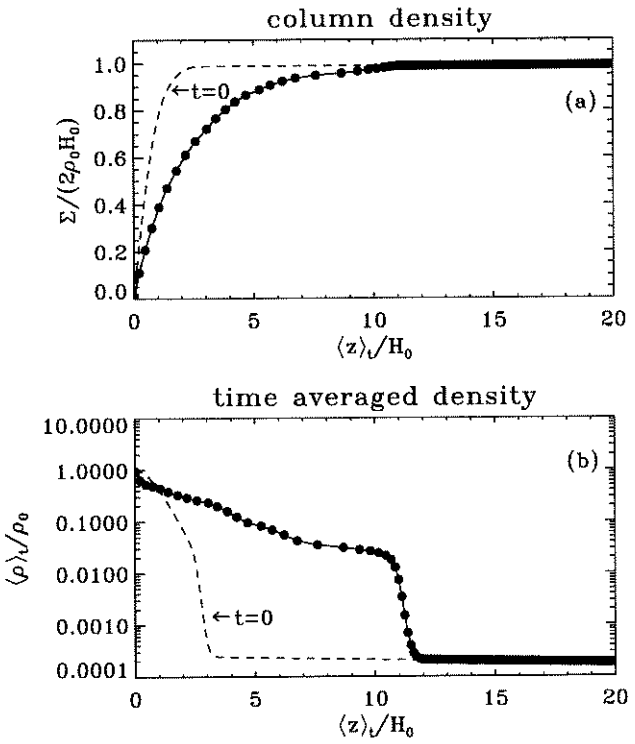

FIG. 4.—(*a*) Column density as a function of the time-averaged position of each Lagrangian fluid element. The dashed line shows the initial distribution. The time average is calculated between $t = 10t_0$ and $t = 40t_0$. The Lagrangian fluid elements have constant enclosed column density as a function of time. By using this property, we evaluate the location of Lagrangian fluid elements from the surface density. Each Lagrangian fluid element is equally spaced at time $t = 0$ with spacing $\Delta z = 0.1H_0$ starting at $z = 0.01H_0$. (*b*) Time average of the density for each fluid element as a function of the time-averaged position of the element. The dashed line shows the initial distribution.

time, because it is proportional to $t\sin(2\pi\nu_0 t)$. However, even if the driving force is symmetric in time, the net momentum in the cloud never remains exactly zero if we use a driving force like the one in equation (31), which is confined to a region near the midplane. The net momentum of the cloud is generated by the nonlinear and nonsymmetric propagation of this disturbance into the stratified cloud, the nonsymmetric restoring forces in the system, and nonsymmetric reflection at the cloud boundary. As disturbances propagate, the restoring force due to the magnetic field is not exactly symmetric in space and time. Also, some of the wave momentum is reflected at the boundary between the cold cloud and hot external medium, and part of it escapes from the cloud. Hence, a net y-component of momentum can and does appear within the cloud, creating a mean motion. We note that if we were modeling a two-dimensional cloud, i.e., the system had finite extent in the y-direction, we could reduce the net drift with a y-distribution of driving force such that the net driving force is zero in the y-direction. Also, if the system was closed in the z-direction, as in a periodic boundary system, it is possible to add momentum in a regulated way so that the net transverse momentum remains exactly zero (e.g., Gammie & Ostriker 1996). However, the combined effects of our 1.5-dimensional approximation, cloud stratification, and open cloud boundary make it difficult to regulate the net drift of the cloud in the y-direction.

Therefore, for our analysis, we divide v_y into two parts. The first is the mean velocity, which shows the mean motion of the entire cloud. The second is the oscillating component of the velocity. We calculate the mean y-component of velocity of the cloud as

$$v_m(t) = \frac{\int_0^{z_f(t)} \rho v_y dz}{\int_0^{z_f(t)} \rho dz} . \tag{41}$$

In this equation, $z_f(t)$ is the full mass position of the cloud, which is defined by

$$\int_0^{z_f(t)} \rho dz = 0.998 \frac{\Sigma_S}{2} , \tag{42}$$

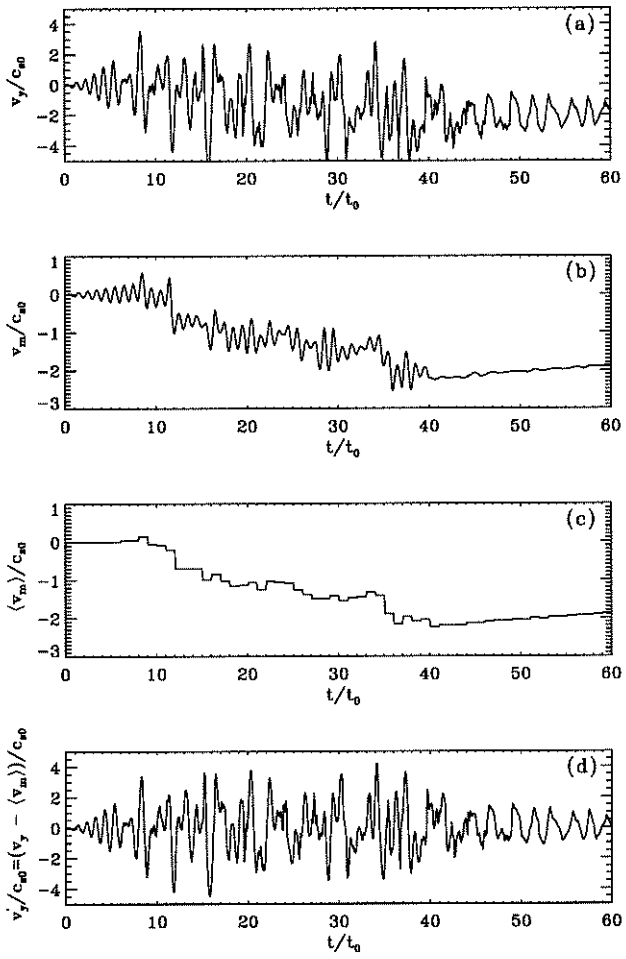

FIG. 5.—Transverse velocities vs. time. (*a*) The *y*-component of the velocity at $z = 0$ as a function of time. (*b*) The mean *y*-component of velocity of the cloud as a function of time. (*c*) The time average of the mean *y*-component of velocity for each cycle of the sinusoidal period of the driving force as a function of time. (*d*) The *y*-component of the velocity at $z = 0$ minus the time average of the mean *y*-component of velocity, as a function of time.

and $z_f(t)$ corresponds to the position of the Lagrangian fluid element which is initially located at $\simeq z_c$, the initial position of the transition region of the temperature. The time evolution of v_m is shown in Figure 5*b*.

Figure 5*b* shows that the mean velocity is still oscillating while the driving force is input ($t = 0 - 40t_0$). In order to remove the oscillation, we take a time average of v_m for each cycle of the sinusoidal period (t_0) of the driving force and define $\langle v_m \rangle$ in the following manner. For example, $\langle v_m \rangle$ between nt_0 and $(n+1)t_0$ is calculated as

$$\langle v_m \rangle (t = nt_0 - (n+1)t_0) = \frac{1}{t_0} \int_{nt_0}^{(n+1)t_0} v_{\rm mean}(t')dt' , \quad (43)$$

where n is an integer. This calculation is done from $n = 0$ to $n = 59$. Figure 5*c* shows $\langle v_m \rangle$ as a function of time. According to the definition, $\langle v_m \rangle$ has the same value between nt_0 and $(n+1)t_0$.

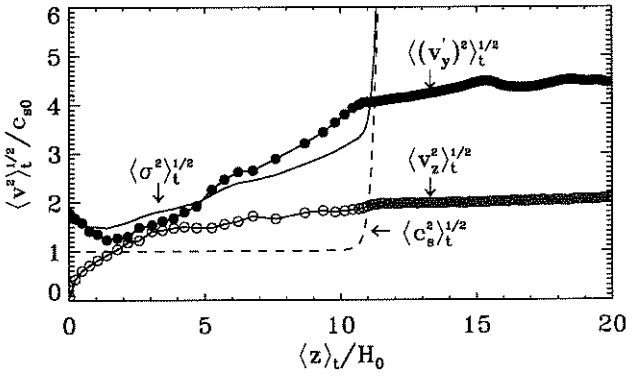

FIG. 6.—Time-averaged rms of various velocities for each Lagrangian fluid element vs. the time average of the position of each element. Open circles show the time-averaged rms of v_z, filled circles show that of v_y', and the dashed line shows the time average of the sound speed. The solid line shows the rms of the time average of the effective one-dimensional velocity dispersion.

Finally, we define the oscillating component of the *y*-velocity as

$$v_y' = v_y - \langle v_m \rangle . \quad (44)$$

Figure 5*d* shows the time evolution of v_y'. In contrast to Figure 5*a*, it is oscillating around $v_y' = 0$.

Figure 6 shows the time average of various velocities for each Lagrangian fluid element plotted versus the time average of the position of each element. Open circles show the time-averaged rms of v_z, filled circles show that of v_y', and the dashed line shows the time average of the sound speed. The solid line shows the rms of the time average of the effective one-dimensional velocity dispersion

$$\sigma = \sqrt{\tfrac{1}{2}[v_z^2 + (v_y')^2] + c_s^2} \quad (45)$$

for each fluid element. The time average is taken between $t = 10t_0$ and $t = 40t_0$. This figure shows that the *y*-component of the velocity is the dominant component in the cloud. The averaged *y*-component of the velocity increases as a function of $\langle z \rangle_t$, except for near the midplane. This means that the largest velocity dispersion occurs in the low-density region. This is a tendency similar to that of linear Alfvén waves. If we assume the WKB approximation and no wave dissipation, the energy flux of the waves is constant, i.e.,

$$\rho (v_y')^2 V_{\rm A} = \text{constant} , \quad (46)$$

where $V_{\rm A}$ is the Alfvén velocity of the background magnetic field, i.e.,

$$V_{\rm A} = \frac{B_z}{(4\pi\rho)^{1/2}} . \quad (47)$$

This leads to

$$v_y' \propto \rho^{-1/4} . \quad (48)$$

Although this relation is not exactly applicable to our nonlinear result, our result shows a similar tendency. We discuss this further in the next section.

3.1.3. *Pressures in the Cloud*

Figure 7*a* shows the time averages of the thermal pressure, magnetic pressure, and dynamic pressures for each Lagrangian fluid element as a function of the time average of the position of each element. The thick dashed line shows the thermal pressure, the thick solid line shows the magnetic pressure of the y-component of the magnetic field, i.e., $B_y^2/8\pi$, the dash-dotted line shows the dynamic pressure for the y-component of velocity, i.e., $\frac{1}{2}\rho(v_y')^2$, and the dotted line shows the dynamic pressure of the z-component of velocity, i.e., $\frac{1}{2}\rho v_z^2$. The thin straight line shows the magnetic pressure of background magnetic field, $B_0^2/8\pi$, and the thin dashed line shows the initial thermal pressure.

In contrast to the WKB theory, the dynamic pressure of the z-component of the velocity is nonzero in our results, although it is smaller than the dynamic pressure of the y-component of the velocity. According to the small-amplitude theory, the dynamic pressure of the y-component of the velocity and the magnetic pressure obey

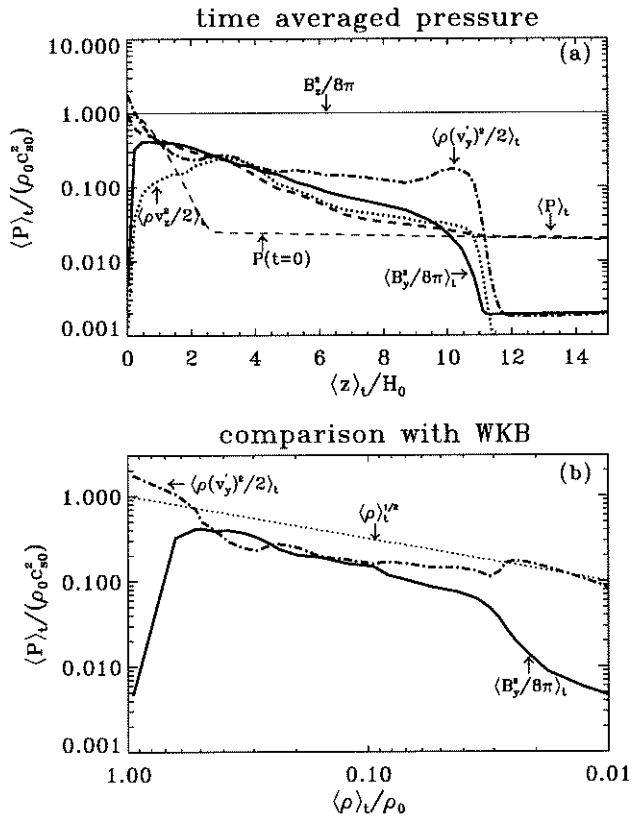

FIG. 7.—(*a*) Time averages of thermal pressure, magnetic pressure, and dynamic pressure for each Lagrangian fluid element as a function of the time-averaged position of each element. The thick dashed line shows the thermal pressure, the thick solid line shows the magnetic pressure of the y-component of the magnetic field, the dash-dotted line shows the dynamic pressure of the y-component of velocity, and the dotted line shows the dynamic pressure of the z-component of velocity. The thin solid line shows the magnetic pressure of background magnetic field, and the thin dashed line shows the initial thermal pressure. (*b*) The dynamic pressure for the y-component of velocity (*dash-dotted line*) and the magnetic pressure of the y-component of the magnetic field (*solid line*) as a function of density. The dotted line shows the scaling expected from the WKB theory. [*See the electronic edition of the Journal for a color version of this figure.*]

equipartition, i.e.,

$$\frac{1}{2}\rho(v_y')^2 = \frac{B_y^2}{8\pi} . \tag{49}$$

Figure 7*a* shows that such an equipartition is almost satisfied between $z = 1H_0$ and $z = 5H_0$, although there are deviations near the midplane. This deviation comes from the effect of a nonzero driving force at $z = 0$ and the symmetrical boundary condition $B_y(z = 0) = 0$. For $z > 5H_0$, a region which contains a small fraction of the total cloud mass (see Fig. 4), the two energies have distinct spatial profiles. Near the interface between the cold and hot material (the cloud boundary), the magnetic pressure decreases more rapidly than expected from the WKB theory. We believe this is due primarily to a standing wave that is set up in the outer cloud, with the cloud boundary acting as a node for B_y and an antinode for v_y'. Although many different wave modes are generated by the turbulence in the cloud, only those that satisfy the boundary condition for a standing wave will interfere constructively upon reflection. A transverse standing wave can be set up even though the boundary itself is moving, since the Alfvén speed is much greater in the outer cloud than the vertical speed of the boundary. The influence of the boundary reaches well inside the cloud, since the effective wavelength of Alfvén waves (scaling as $\rho^{-1/2}$ for waves of fixed frequency) is also quite large in the low-density region. For example, at $z = 5H_0$, where $\rho \simeq 0.1\rho_0$, Alfvén waves of the input frequency $\nu_0 = c_{s0}/H_0$ have wavelength $\lambda \simeq 4.5H_0$; at $z = 10H_0$, it increases to $\lambda \simeq 8H_0$. An important result is that even though the waves are quasi-linear in the outer cloud ($B_y \ll B_0$), the transverse velocity amplitude is much larger than expected from equipartition arguments.

In Figure 7*b* we show the dynamic pressure of the y-component of velocity and the magnetic pressure of the y-component of the magnetic field as a function of density in order to compare with the WKB model predictions.

We find that the energy in transverse velocities, $\frac{1}{2}\rho(v_y')^2$, scales approximately as $\rho^{1/2}$ in the outer cloud, the same as the WKB theory, although there is a noticeable upward turn at $z \simeq 9H_0$ due to the standing wave effect. However, the wave magnetic energy $B_y^2/(8\pi)$, which is directly responsible for vertical support, decreases more rapidly than in the WKB model in the outer cloud, scaling approximately as ρ. We note that strict adherence to the WKB predictions is not expected in our model due to nonlinearity, wave dissipation, and the low-frequency $\nu_0 = c_{s0}/H$ of the input turbulence.

3.1.4. *Energies in the Cloud*

Figure 8 shows the time evolution of various energies in the cloud. These are calculated as follows: kinetic energy of the z-component of velocity

$$E_{kz}(t) = \int_0^{z_f(t)} \tfrac{1}{2}\rho v_z^2 dz , \tag{50}$$

kinetic energy of the y-component of velocity

$$E_{ky}(t) = \int_0^{z_f(t)} \tfrac{1}{2}\rho v_y^2 dz - E_{km} , \tag{51}$$

where E_{km} is the kinetic energy of the mean motion of the

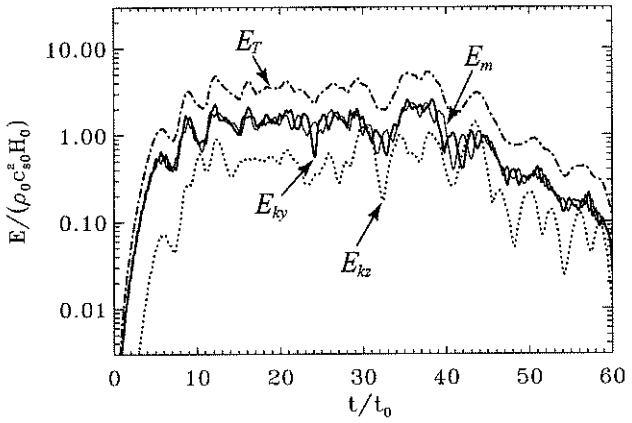

FIG. 8.—Time evolution of various energies in the cloud. The thick solid line shows E_{ky}, the dotted line shows E_{kz}, the thin solid line shows E_m, and the dash-dotted line shows E_T. The values of each energy are smoothed out over every one cycle of the driving force in order to remove periodic oscillations originating from the driving force. [*See the electronic edition of the Journal for a color version of this figure.*]

cloud, i.e.,

$$E_{km}(t) = \tfrac{1}{2}\langle v_m \rangle^2 \int_0^{z_f(t)} \rho dz \; ; \tag{52}$$

magnetic energy of the y-component of magnetic field

$$E_m(t) = \int_0^{z_f(t)} \frac{B_y^2}{8\pi} dz \; ; \tag{53}$$

and the sum of the above terms

$$E_T(t) = E_{kz}(t) + E_{ky}(t) + E_m(t) \; . \tag{54}$$

In the above equations, the integration was done from 0 to $z_f(t)$ because we are interested in energies of the cold material. Strictly speaking, the total energy in each case is twice the value we calculate because of the mirror-symmetric boundary condition at $z = 0$. Equation (51) shows that the mean kinetic energy of the cloud is subtracted from the kinetic energy of y-component of velocity, so that E_{ky} means the kinetic energy of the oscillating velocity.

In Figure 8 the thick solid line shows E_{ky}, the dotted line shows E_{kz}, the thin solid line shows E_m, and the dashed-dotted line shows E_T. The values of each energy are smoothed out over every one cycle of the driving force in order to remove periodic oscillations originating from the driving force. Among the energies, E_{ky} and E_m are comparable to each other, but E_{kz} is significantly smaller than the others. The sum of energies E_T is almost constant in a logarithmic scale while the input energy is constant ($t = 10t_0$–$40t_0$), although it has some fluctuations. After the driving force is terminated at $t = 40t_0$, the energies decrease almost exponentially. The decreasing time is $\simeq 8.5t_0$.

3.2. *Parameter Dependence on the Strength of the Driving Force*

3.2.1. *Density, Velocity, and Pressure*

In this paper we study the effect of changing the strength of the driving force by changing a_d in equation (31).

Figure 9 shows the time evolution of densities for $\tilde{a}_d = 20$ and $\tilde{a}_d = 40$. The y-velocities at $z = 0$, v_y' are also shown in the figure. This figure shows that a stronger driving force causes a larger turbulent velocity, which results in a more dynamic evolution of the molecular cloud, including stronger shock waves and larger excursions of the cloud boundary. However, after terminating the driving force at $t = 40t_0$, the shock waves dissipate and the clouds shrink in both cases.

Figure 10 shows the time average of the density and velocities for each Lagrangian fluid element for $\tilde{a}_d = 20$ and $\tilde{a}_d = 40$. The time average is taken between $t = 10t_0$ and $t = 40t_0$. This figure also shows that a stronger driving force causes the cloud to move further outward and a larger velocity dispersion within the cloud.

Figure 11 shows the time average of pressures for $\tilde{a}_d = 20$ and $\tilde{a}_d = 40$. When the driving force is strong, the magnetic pressure and dynamic pressure of the z-component of velocity become significantly larger than the thermal pressure.

3.2.2. *Energy*

Figure 12 shows the time evolution of E_T for both $\tilde{a}_d = 20$ and $\tilde{a}_d = 40$. These values are also smoothed out over every one cycle of the driving force to remove periodic oscillations. In the case of $\tilde{a}_d = 20$, the energy is almost constant in a logarithmic scale while the driving amplitude is constant ($t = 10t_0$–$40t_0$). However, in the case of $\tilde{a}_d = 40$, the energy is still gradually increasing until $t = 30t_0$, but afterward becomes almost constant until $t = 40t_0$. After terminating the driving force at $t = 40t_0$, both energies decrease almost exponentially. The energy decreasing times, t_d, for each parameter, which are estimated by fitting an exponential function, are listed in Table 1. In this study, we terminate the driving force at $t = 40t_0$ in every case for simplicity. However, we found that the energy decreasing time can vary somewhat depending on when we terminate the driving force. Accounting for this as well as the fitting error of the exponential function, we conclude that the energy decreasing times have a range of variation about $\pm 2t_0$ of the values listed in Table 1.

3.2.3. *Correlations between Velocities and Sizes*

Here we investigate the correlation between the velocity dispersion and the height of the cloud. Figure 13*a* shows the time-averaged velocity dispersions $\langle \sigma^2 \rangle_t^{1/2}$ of different Lagrangian fluid elements for different $\tilde{a}_d$, as a function of $\langle z \rangle_t$. The open circles correspond to Lagrangian fluid elements whose initial positions are located at $z = 2.51H_0$,

TABLE 1

DISSIPATION TIME AS A FUNCTION OF $\tilde{a}_d$

		$z(t=0) = 2.51H_0$		$z(t=0) = 0.61H_0$	
$\tilde{a}_d$	t_d/t_0	$\langle z \rangle_t/H_0$	$\langle \sigma^2 \rangle_t^{1/2}/c_{s0}$	$\langle z \rangle_t/H_0$	$\langle \sigma^2 \rangle_t^{1/2}/c_{s0}$
10.....	9.0	4.00	2.54	0.76	1.18
20.....	5.5	6.82	3.73	1.13	1.54
30.....	8.5	10.8	4.65	1.78	1.92
40.....	9.0	17.9	5.73	2.91	2.47
50.....	15.0	17.4	5.99	3.34	2.68

NOTE.—Time-averaged height and time-averaged velocity dispersion as a function of $\tilde{a}_d$ for two Lagrangian elements: $z(t=0) = 2.51H_0$, approximately the full-mass position, and $z(t=0) = 0.61H_0$, approximately the half-mass position.

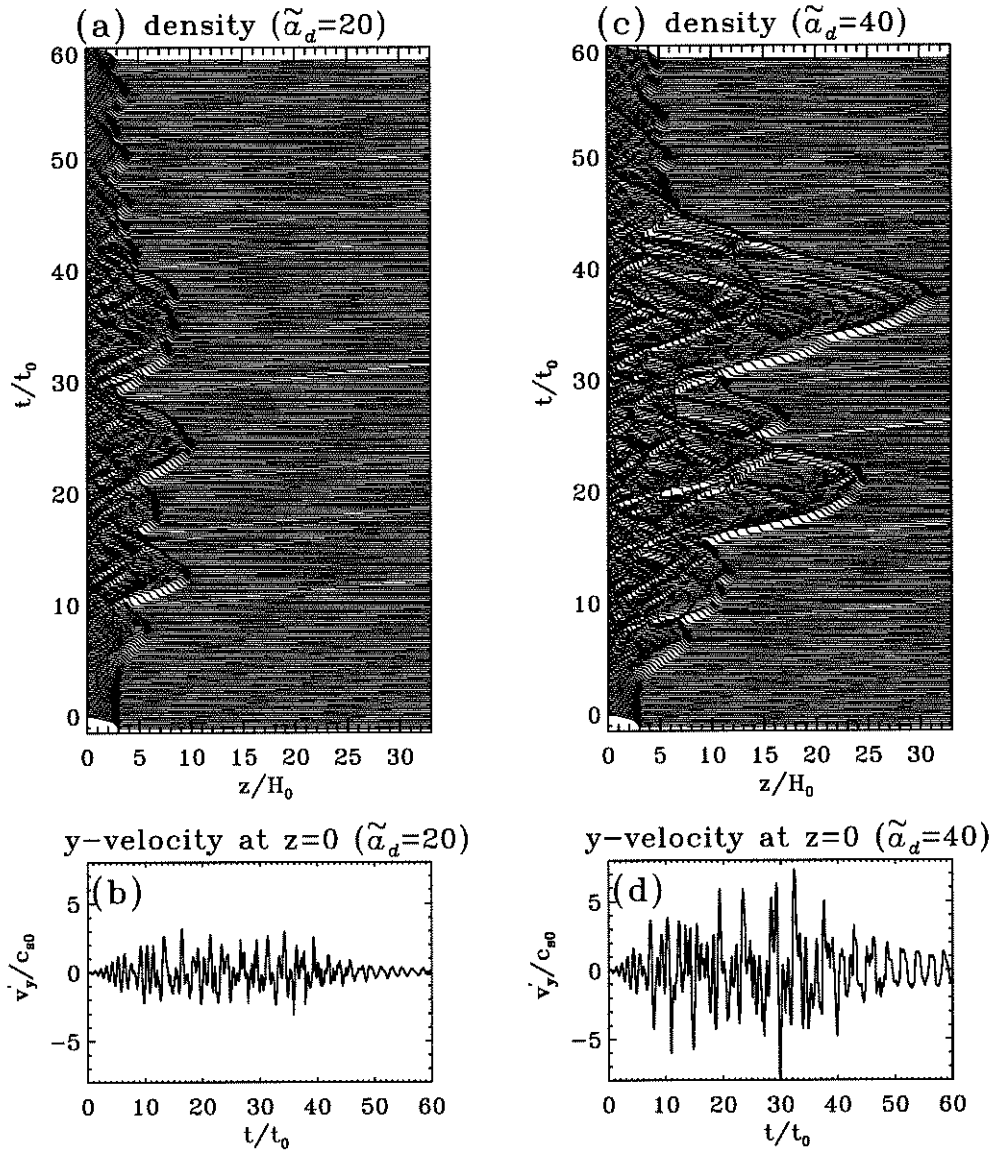

FIG. 9.—Evolution of clouds with $\tilde{a}_d = 20$ and $\tilde{a}_d = 40$. (*a*) Time evolution of densities for $\tilde{a}_d = 20$. (*b*) The oscillating part of *y*-velocity at $z = 0$, v'_y, as a function of time for $\tilde{a}_d = 20$. (*c*) Time evolution of densities for $\tilde{a}_d = 40$. (*d*) The oscillating part of *y*-velocity at $z = 0$, v'_y, as a function of time for $\tilde{a}_d = 40$. The density plots at various times are stacked with time increasing upward in uniform increments of $0.2t_0$.

which is close to the edge of the cold cloud. The filled circles corresponds to Lagrangian fluid elements whose initial positions are located at $z = 0.61H_0$, which is approximately the half-mass position of the cold cloud. Each circle corresponds to a different value of $\tilde{a}_d$. These values are summarized in Table 1. The dotted line shows

$$\langle \sigma^2 \rangle_t^{1/2} \propto \langle z \rangle_t^{0.5} . \tag{55}$$

This figure shows that the velocity dispersions have a good correlation with the heights of the molecular clouds.

Figure 13*b* shows the correlation between the velocity dispersion and mean Alfvén velocity of the cloud $\bar{V}_A$ at the mean position $\langle z \rangle_t$ of the Lagrangian elements. The dotted line shows

$$\langle \sigma^2 \rangle_t^{1/2} \propto \bar{V}_A . \tag{56}$$

This figure shows that the velocity dispersions have a good correlation with the mean Alfvén velocity, defined by

$$\bar{V}_A \equiv \frac{B_0}{\sqrt{4\pi\bar{\rho}}} , \tag{57}$$

where

$$\bar{\rho} = \frac{\Sigma}{2\langle z \rangle_t} \tag{58}$$

is the mean density and Σ is the column density for each

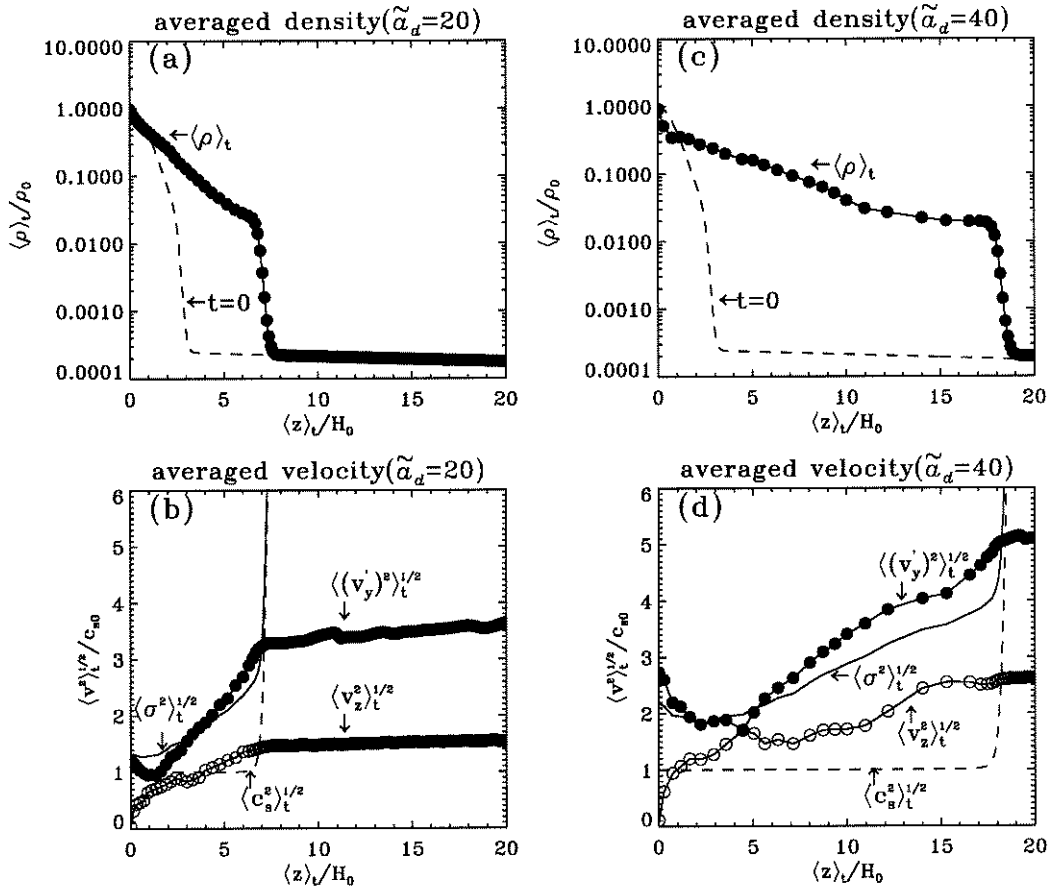

FIG. 10.—Density and velocity dispersions for the cases $\tilde{\alpha}_d = 20$ and $\tilde{\alpha}_d = 40$. (*a*) Time average of the density for each element as a function of the time-averaged position of each element for $\tilde{\alpha}_d = 20$. The time average is calculated between $t = 10t_0$ and $t = 40t_0$. Each Lagrangian fluid element is equally spaced at time $t = 0$ with spacing $\Delta z = 0.1H_0$ starting at $z = 0.01H_0$. (*b*) The time-averaged rms of various velocities for each Lagrangian fluid element plotted vs. the time average of the position of each element for $\tilde{\alpha}_d = 20$. Open circles show the time-averaged rms of v_z, filled circles show that of v_y', and the dashed line shows the time average of the sound speed c_s. The solid line shows the rms of the time average of the effective one-dimensional velocity dispersion. (*c*) The time average of the density for each element as a function of the time-averaged position of each element for $\tilde{\alpha}_d = 40$. (*d*) The time-averaged rms of various velocities for each Lagrangian fluid element plotted vs. the time average of the position of each element for $\tilde{\alpha}_d = 40$.

Lagrangian element. We discuss the meaning of these correlations in the next section.

4. DISCUSSION

4.1. *Velocity Dispersion and Equilibrium*

In Figure 13*a* we found that the velocity dispersion obeys the line-width–size relation

$$\langle\sigma^2\rangle_t^{1/2} \propto \langle z\rangle_t^{0.5} . \tag{59}$$

This relation is satisfied (at both the full-mass and half-mass Lagrangian positions) for an ensemble of the clouds with different strengths of the driving force. It is consistent with observational results of molecular clouds (Larson 1981; Myers 1983; Solomon et al. 1987). Within any individual cloud, $\langle\sigma^2\rangle_t^{1/2}$ also increases toward the cloud boundary.

A similar but not identical relation, relating the velocity dispersion at $z = 0$ to the size of the cloud, is expected in virtually any one-dimensional model, regardless of the form of spatial variation of the pressure within the cloud. This is because an integral over the vertical force-balance equation reveals that the total pressure at $z = 0$, $P_{\rm tot,0}$ must equal the weight of the accumulated gas above, $\pi G\Sigma^2/2$, assuming that the surface pressure is negligible. If $P_{\rm tot,0} = \rho_0\sigma_{\rm eff,0}^2$, where $\sigma_{\rm eff,0}$ is the effective velocity dispersion at $z = 0$, and $\Sigma = 2\rho_0 Z$, in which Z is the typical size scale of the cloud, then one naturally obtains

$$\sigma_{\rm eff,0} \propto Z^{1/2} \tag{60}$$

for an ensemble of clouds of fixed total column density Σ but varying $\sigma_{\rm eff,0}$. This relation applies to the Spitzer equilibrium state, in which $\sigma_{\rm eff,0} = c_s$ and $Z = H_0$. It also applies to the equilibrium state calculated by Martin et al. (1997), in which $\sigma_{\rm eff,0}$ is the effective velocity dispersion associated with Alfvén waves at $z = 0$. While a similar relation will inevitably apply to our nonlinear model as well, we note that the relation (59) is more general, in that it relates the velocity dispersion *at* the position (not $z = 0$) of a Lagrangian mass element to the position of that element. This more general correlation is a less predictable property of our time-averaged equilibrium state. It is also closer to what is often measured, since optical depth effects may mean that a measured velocity dispersion samples the largest scales of an observed cloud rather than the center.

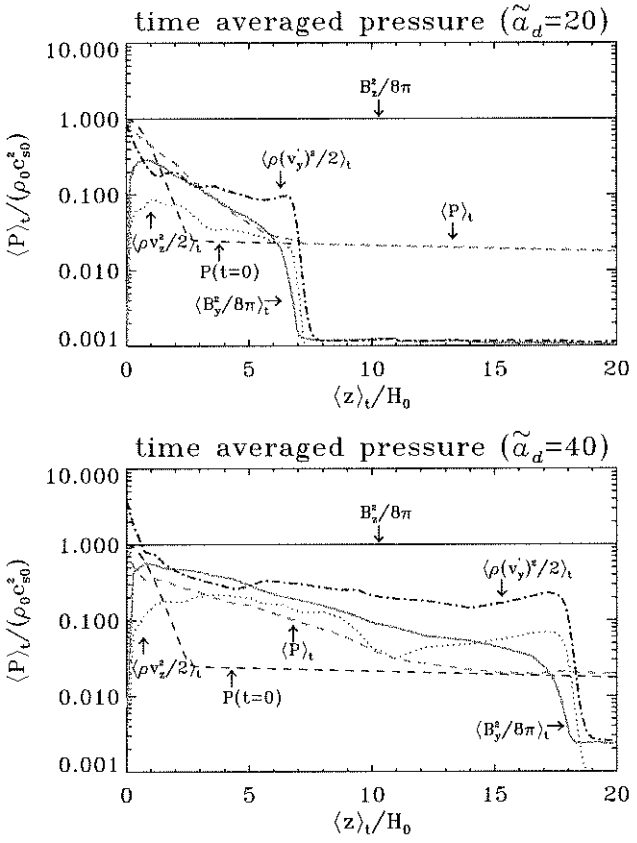

FIG. 11.—Time averages of the thermal pressure, magnetic pressure, and dynamic pressures for each Lagrangian fluid element as a function of the time-averaged position of each element. The upper panel is for $\tilde{a}_d = 20$ and the lower panel is for $\tilde{a}_d = 40$. The thick dashed line shows the thermal pressure, the thick solid line shows the magnetic pressure of the y-component of the magnetic field, the dash-dotted line shows the dynamic pressure of the y-component of velocity, and the dotted line shows the dynamic pressure of the z-component of velocity. In both panels the thin solid line shows the magnetic pressure of background magnetic field and the thin dashed line shows the initial thermal pressure. [*See the electronic edition of the Journal for a color version of this figure.*]

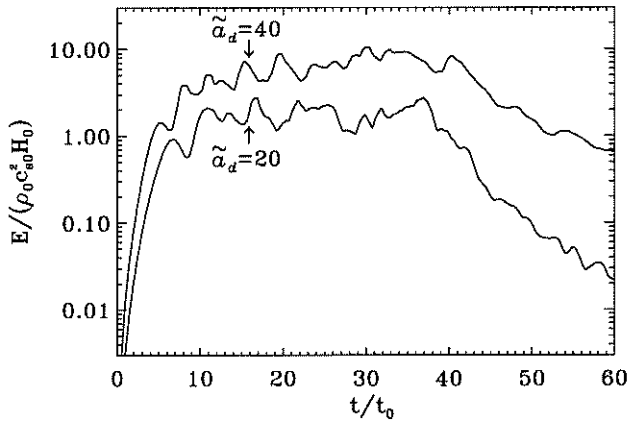

FIG. 12.—Time evolution of E_T for both $\tilde{a}_d = 20$ and $\tilde{a}_d = 40$. The values of each energy are smoothed out over every one cycle of the driving force in order to remove periodic oscillations originating from the driving force.

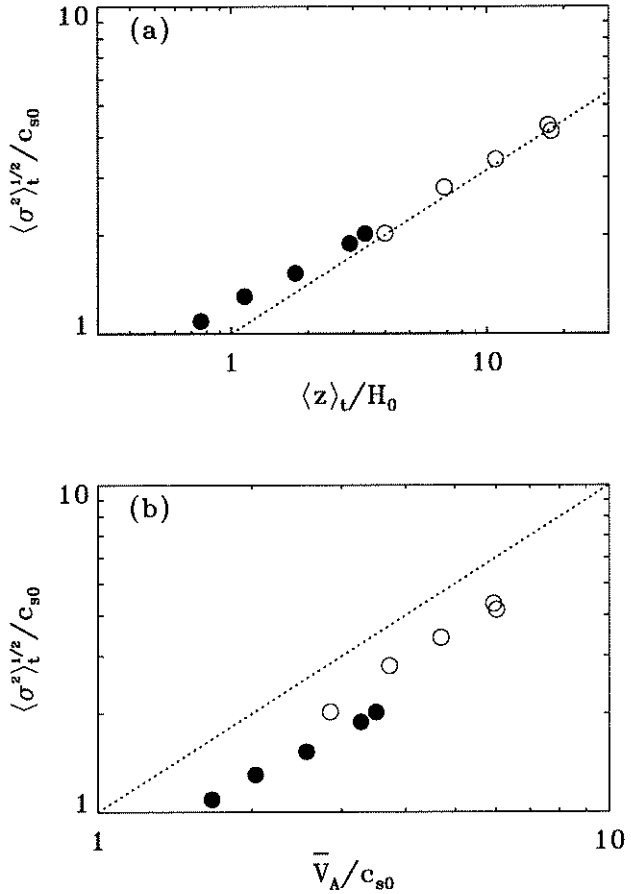

FIG. 13.—Global properties of an ensemble of clouds with different driving strengths $\tilde{a}_d$. (*a*) Time-averaged velocity dispersions of different Lagrangian fluid elements for different $\tilde{a}_d$, as a function of time-averaged positions. The open circles correspond to Lagrangian fluid elements whose initial positions are located at $z = 2.51H_0$, which is close to the edge of the cold cloud. The filled circles correspond to Lagrangian fluid elements whose initial positions are located at $z = 0.61H_0$, which is approximately the half-mass position of the cold cloud. The dotted line shows $\langle\sigma^2\rangle_t^{1/2} \propto \langle z\rangle_t^{0.5}$. Each circle can be associated with a particular model in our study by comparison with the numbers in Table 1. (*b*) Time-averaged velocity dispersions as a function of the mean Alfvén velocity of the cloud. The dotted line shows $\langle\sigma^2\rangle_t^{1/2} \propto \bar{V}_A$.

Equation (59) is strongly related to another relation,

$$\langle\sigma^2\rangle_t^{1/2} \propto \bar{V}_A\,, \tag{61}$$

which is shown in Figure 13*b*, once more for both the half-mass and full-mass positions for our ensemble of clouds. This relation is also consistent with observational results of molecular clouds (Crutcher 1999; Basu 2000). For example, Figure 1*b* of Basu (2000) shows an excellent correlation between the line-of-sight component of the large-scale magnetic field B_{los} and $\sigma\rho^{1/2}$ for observed clouds of widely varying values of ρ, B_{los}, and σ, essentially the same correlation as equation (61) if $B_{los} \propto B$ on average.

Here we would like to point out that the relation (61) does not necessarily imply that turbulent motions are due to Alfvén waves, although that is primarily the case in our simulation. The relation is far more general in that it is obtained when the velocity dispersion is caused by any mechanism

which results in the clouds being in virial balance between gravitational and turbulent energies, as well as having a mass-to-flux ratio that is approximately uniform from cloud to cloud (Mouschovias 1987; Shu et al. 1987). Rather than imagining a time-independent mean Alfvén speed in a cloud (strictly true in an incompressible medium or a periodic box simulation with a fixed mean density) and turbulent motions becoming comparable to that speed, our simulation reveals that it is the mean Alfvén speed of any cloud that readjusts to a new value as $\bar{\rho}$ drops to accommodate a particular level of turbulent driving. In this view, the turbulent dispersion σ is the more fundamental quantity, dependent on the particular source of driving, and $\bar{V}_A$ is a quantity which readjusts to become comparable to σ.

Finally, we note that the relation (61) depends on the definition of the mean Alfvén velocity. If we use the local Alfvén velocity of each particle, we could not get a clear correlation like equation (61). The mean Alfvén velocity is often calculated observationally using the mean density, as in equations (57) and (58), because it is difficult to directly measure a local Alfvén velocity. The local Alfvén velocity in a gravitationally stratified cloud often takes on values much different than the overall mean quantity $\bar{V}_A$ used in equation (61). For example, the time-averaged local Alfvén velocity near the edge of the cloud is about 2.6 times greater than $\bar{V}_A$ for the case of $\tilde{a}_d = 30$.

4.2. *Relation to Linear Model and Chandrasekhar-Fermi Formula*

In our simulation, the velocity component parallel to the background magnetic field (v_z) is generated by the nonlinear effect of the waves. However, the time-averaged magnitude of v_z is significantly less than the time-averaged magnitude of v_y' in all our models (see Figs. 6, 7, 10, and 11). Although the waves are nonlinear, the coupling between the Alfvén and slow-mode MHD waves is not so strong as to destroy an approximate equipartition between $B_y^2/(8\pi)$ and $\frac{1}{2}\rho(v_y')^2$ throughout much of the cloud, which is the expected result for purely transverse linear Alfvén waves. However, this equipartition does break down in the outer part of the cloud, where standing wave motions are established in which B_y has a node at the cloud boundary and v_y' has an antinode.

The breakdown of the v_y' versus B_y relation in outer cloud means that the original Chandrasekhar-Fermi formula breaks down there as well. If we assume that the dispersion of polarization angle of the magnetic field ($\delta\theta$) is related to the velocity dispersion as

$$\delta\theta = \frac{|B_y|}{B_0} = \alpha\frac{|v_y'|}{V_A}, \tag{62}$$

we can estimate the strength of the magnetic field of the cloud by using the observational values of polarization angle, density, and velocity dispersion. This yields

$$B_0 = \alpha(4\pi\rho)^{1/2}|v_y'|(\delta\theta)^{-1}, \tag{63}$$

where α is a nondimensional factor and equals 1 for linear Alfvén waves. The relation (63) with $\alpha = 1$ was proposed by Chandrasekhar & Fermi (1953) in order to estimate the strength of the background magnetic field in the interstellar medium. The generalized form with $\alpha \neq 1$ can be fit to our simulation if we define α in our simulation as the square root of the ratio of time-averaged magnetic pressure to dynamic pressure for each Lagrangian fluid element, i.e.,

$$\alpha = \left(\frac{\langle B_y^2/(8\pi)\rangle_t}{\langle\rho(v_y')^2/2\rangle_t}\right)^{1/2}. \tag{64}$$

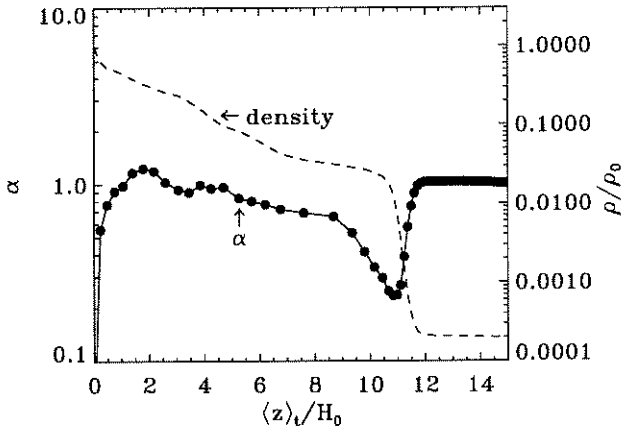

FIG. 14.—Parameter α, which appears in the Chandrasekhar-Fermi formula (eq. [63]), as a function of the time-averaged position of fluid elements within the cloud for the case of $\tilde{a}_d = 30$. The time-averaged density, which was shown in Fig. 4, is also shown as a dashed line, mainly to clarify the position of the edge of the cloud.

The resulting distribution of α as a function of $\langle z\rangle_t$ for the case of $\tilde{a}_d = 30$ is shown in Figure 14. The time-averaged density, which was shown in Figure 4, is also shown as a dashed line to clarify the edge of the cloud. It shows that α is close to unity inside the cloud in the region where most of the mass is enclosed (see Fig. 4), but it decreases near the surface of the cold cloud, where the standing wave effect becomes important; the minimum value is about $\alpha = 0.23$. Outside of the cloud ($\langle z\rangle_t > 12H_0$ in Fig. 14), $\alpha = 1$ since the waves are linear there due to the low density and high ambient Alfvén speed. Therefore, while our nonlinear model supports the use of the Chandrasekhar-Fermi formula throughout most of a stratified cloud, we caution against its use with $\alpha = 1$ near the surface of a cloud.

4.3. *Global Oscillations*

Figure 15 shows the time evolution of the position of a Lagrangian fluid element whose initial position is $z = 2.51$, for the standard model with driving strength $\tilde{a}_d = 30$. This corresponds to the motion of the outer edge of the cloud. The motions resemble longitudinal normal mode oscillations, with the excursions of the outer cloud very similar to free-fall. The dotted line in the figure shows the trajectory for free-fall motion of the fluid element for several different time intervals. The peak of the trajectories are chosen to coincide with a peak of the oscillation in the computed model. The paths are parabolic as a result of the constant gravity acting on a comoving mass shell in the one-dimensional approximation. Similar to the transverse standing wave that is set up in the outer cloud, the longitudinal motions in this region also resemble a standing wave pattern with an antinode of v_z at the cloud boundary. The outermost part of the cloud suffers the greatest displacements, as in the case of a pulsating star. Once the internal

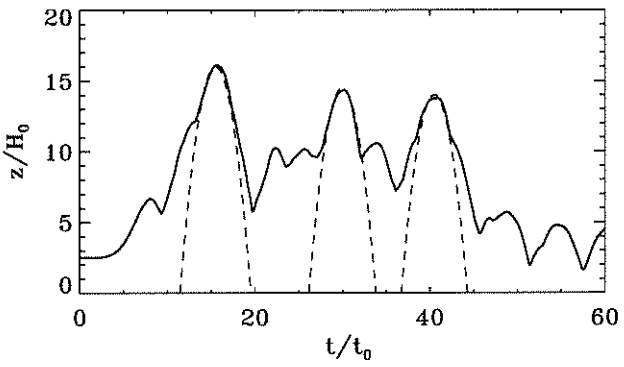

FIG. 15.—Time evolution of the position of a Lagrangian fluid element whose initial position is located at $z = 2.51H_0$ for the case of $\tilde{a}_d = 30$. The dotted line shows the trajectories of free-fall motion for the element.

driving is discontinued ($t > 40t_0$), the outer surface also moves inward in nearly a free-fall manner.

Figures 3 and 15 also show that some residual oscillations remain on the largest scale even after the damping of most of the internal turbulent energy. This effect is reminiscent of the recent observation of Lada et al. (2003) that implied a global oscillation of Barnard 68, a cloud with only subsonic internal turbulence. We hypothesize that Barnard 68 may have dissipated most of the internal turbulence left over from its formation but that only a large-scale oscillation remains, as in the late stage of our simulation after turbulent driving is discontinued. However, we caution that ours is a one-dimensional model and that globally coherent standing-wave motions need to be demonstrated in a multidimensional model.

4.4. *Dissipation of Energy*

The dissipation of energy that we input into nonlinear transverse Alfvén modes is caused by either shock waves or grid-scale dissipation, which is similar to the results of Stone et al. (1998). In addition to the dissipation, a part of the energy escapes from the cloud in our simulation. We measured the Poynting flux, which is the dominant energy flux, at the full-mass position and the 20% mass position, which is just outside the region we input the driving force. The time integral of the Poynting flux at the full-mass position is about 30% of that at the 20% mass position.

In our model, the majority of dissipation occurs due to the transfer of energy to small scales via nonlinear steepening and/or a turbulent cascade, followed by damping on the grid scale through numerical resistivity. This is because the kinetic energy of longitudinal motions, which are the cause of shock waves, is smaller than that of transverse motions. The primary dissipation of Alfvénic motions then, is not due to coupling to slow modes, although this is present at a significant level. This is similar to the finding of the one-dimensional numerical model of Gammie & Ostriker (1996), although the same authors claim that in a multi-dimensional simulation, compressive effects become a major source of dissipation (Stone et al. 1998); however, see Cho & Lazarian (2003), who find that the primary dissipation mechanism in a three-dimensional simulation is not the coupling of Alfvén modes to slow and fast modes.

So if the primary source of dissipation in this simulation is grid-scale dissipation after nonlinear steepening of waves (and perhaps some cascade to smaller wavelengths), then is the dissipation rate a physical effect or an artifact of the simulations? To answer this, we have increased the resolution of our numerical simulations until the dissipation rate is nearly independent of grid size for the case of the typical parameter. Hence, the numerical diffusion is no longer resolution-determined at our current resolution of 50 points per initial scale height in the region where most of the mass is located. If we use a smaller grid size, the final scale of the dissipation is smaller, but the rate of dissipation stays nearly the same. In reality, there must be a physical effect such as ion-neutral friction that would damp the waves at small scales.

The dissipation time of our results are a few crossing times of the time-averaged scales of the clouds (see Table 1). They are a bit longer than estimated from periodic box simulations. We think that this comes from the generation of longer wavelength modes as the waves travel to low-density regions near the cloud's surface. However, it is already known that one-dimensional simulations have lower dissipation rates than two- or three-dimensional ones (Ostriker et al. 2001). Therefore, higher dimensional global simulations will give the final answer in the future.

4.5. *Future Work*

This is the first in a series of papers. In the next paper, we will conduct a complete survey of the effect of important parameters such as β_0 and ν_0. Additionally, the study of random, rather than sinusoidal, disturbances will be considered. Moreover, we will study the case of circularly polarized Alfvén waves by including an x-component of motions in the simulation. A circularly polarized wave is possibly less dissipative than a linearly polarized wave, since in the theoretical limit of an infinite wave train, a flux of circularly polarized waves has no associated magnetic pressure gradient and thereby induces no compression of gas. Although conversion of Alfvén modes to slow modes is already not a dominant source of dissipation in our model, it will be useful to see if the dissipation rate is even less than measured here when circularly polarized waves propagate in a finite-sized cloud.

We also expect to include ion-neutral friction in a future simulation. This effect is expected to be important in molecular clouds, especially in this model as a damping mechanism of Alfvén waves (Kulsrud & Pearce 1969; Zweibel & Josafatsson 1983). It would also change the density structure of a cloud lifted up by wave pressure, as demonstrated in the case of linear Alfvén waves by Martin et al. (1997).

Finally, we believe that a multidimensional turbulent simulation in a gravitationally stratified medium is very necessary for the future, especially to obtain more definitive dissipation rates in a stratified cloud and to study the feedback to turbulence due to gravitational contraction and differential rotation.

5. SUMMARY

We have performed a numerical simulation of nonlinear MHD waves in a stratified molecular cloud. Our main results are as follows:

1. Because of the effective pressure of MHD turbulence, our one-dimensional cloud is lifted upward and establishes a steady state characterized by oscillations around a time-

averaged equilibrium state. The outer, low-density parts of the cloud undergo the largest oscillations, which have the character of free-fall motions. After turbulent driving is discontinued, the cloud falls back toward the initial equilibrium, but some large-scale oscillations of the cloud are the longest lived modes.

2. The nonlinear effect of the wave propagation results in a significant conversion of energy from Alfvén waves to compressive slow (acoustic) modes and consequent shock formation. However, the energy in transverse modes always remains significantly greater than that in longitudinal modes. Further dissipation of transverse modes takes place through the generation of smaller scale structure through nonlinear steepening or a cascade, culminating in resistive dissipation on the grid scale.

3. Within each cloud, the magnetic pressure associated with wave motion, $\langle B_y^2/(8\pi)\rangle_t$, is in approximate equipartition with the kinetic energy in transverse motions $\langle \rho(v_y')^2/2\rangle_t$ in the region containing most of the mass. However, in the low-density outer regions, the wave amplitudes have the character of standing waves, such that B_y has a node and v_y' has an antinode. All of this means that the Chandrasekhar-Fermi model applied to a stratified cloud will have a multiplicative constant α that is ≈ 1 with weak spatial dependence through much of the cloud but drops to much lower values near the edge of the cloud.

4. After turbulent driving is discontinued, the dissipation time of the cloud turbulence is $\sim 10 t_0$ or several crossing times of the time-averaged equilibrium state during turbulent driving. These times are up to a few times longer than those found in multidimensional periodic simulations. This would be due partly to fewer dissipation avenues in a one-dimensional approximation but also partly to the generation of long-wavelength modes due to the cloud stratification.

5. For an ensemble of clouds with different levels of internal driving, we find the relation $\sigma \propto Z^{0.5}$, where σ is the time-averaged one-dimensional velocity dispersion measured at a size scale Z of the time-averaged equilibrium state of the cloud.

6. For the same ensemble of clouds, the above relation also implies that $\sigma \propto \bar{V}_A$, where $\bar{V}_A$ is the mean Alfvén velocity determined from the mean density of the cloud. This relation is in agreement with observed properties of magnetized clouds and cloud cores.

T. K. acknowledges support due to a Fellowship from the Canadian Galactic Plane Survey, which is supported by a Natural Sciences and Engineering Research Council of Canada (NSERC) Collaborative Research Opportunities Grant. T. K. also benefited from a Fellowship from SHARCNET, a high-performance computing project funded by ORDCF and CFI/OIT. S. B. was supported by an individual research grant from NSERC. Numerical computations were carried out mainly on the VPP5000 at the Astronomical Data Analysis Center of the National Astronomical Observatory, Japan.

REFERENCES

Arons, J., & Max, C. E. 1975, ApJ, 196, L77
Basu, S. 2000, ApJ, 540, L103
Blitz, L., & Williams, J. P. 1999, in The Origin of Stars and Planetary Systems, ed. C. J. Lada & N. Kylafis (Dordrecht: Kluwer), 3
Chandrasekhar, S. 1951, Proc. R. Soc. London A, 210, 26
Chandrasekhar, S., & Fermi, E. 1953, ApJ, 118, 113
Cho, J., & Lazarian, A. 2003, MNRAS, in press
Cohen, R. H., & Kulsrud, R. M. 1974, Phys. Fluids, 17, 2215
Crutcher, R. M. 1999, ApJ, 520, 706
Dewar, R. L. 1970, Phys. Fluids, 13, 2710
Falgarone, E., & Puget, J. L. 1986, A&A, 162, 235
Fatuzzo, M., & Adams, F. C. 1993, ApJ, 412, 146
Gammie, C. F., & Ostriker, E. C. 1996, ApJ, 466, 814
Goldreich, P., & Kwan, J. 1974, ApJ, 189, 441
Goldsmith, P. F., & Langer, W. D. 1978, ApJ, 222, 881
Goodman, A. A., Bastien, P., Myers, P. C., & Ménard, F. 1990, ApJ, 359, 363
Hollweg, J. V. 1992, ApJ, 389, 731
Hollweg, J. V., Jackson, S., & Galloway, D. 1982, Sol. Phys., 75, 35
Jeans, J. H. 1928, Astronomy and Cosmogony (Cambridge: Cambridge Univ. Press)
Kudoh, T., Matsumoto, R., & Shibata, K. 1999, Comput. Fluid. Dyn. J., 8, 56
Kudoh, T., & Shibata, K. 1999, ApJ, 514, 493
Kulsrud, R., & Pearce, W. P. 1969, ApJ, 156, 445
Lada, C. J., Bergin, E. A., Alves, J. F., & Huard, T. L. 2003, ApJ, 586, 286
Larson, R. B. 1981, MNRAS, 194, 809
Mac Low, M.-M. 1999, ApJ, 524, 169
Mac Low, M.-M., Klessen, R. S., Burkert, A., & Smith, M. D. 1998, Phys. Rev. Lett. 80, 2754
Mariska, J. T., & Hollweg, J. V. 1985, ApJ, 296, 746
Martin, C. E., Heyvaerts, J., & Priest, E. R. 1997, A&A, 326, 1176
Matthews, B. C., & Wilson, C. D. 2002, ApJ, 574, 822
McKee, C. F., & Zweibel, E. G. 1995, ApJ, 440, 686
Mestel, L. 1965, QJRAS, 6, 161
Mouschovias, T. Ch. 1975, Ph.D. thesis, Univ. California, Berkeley
———. 1987, in Physical Processes in Interstellar Clouds, ed. G. E. Morfill & M. Scholer (Dordrecht: Reidel), 453
Mouschovias, T. Ch., & Spitzer, L., Jr. 1976, ApJ, 210, 326
Myers, P. C. 1983, ApJ, 270, 105
Nakano, T., & Nakamura, T. 1978, PASJ, 30, 671
Ostriker, E. C., Gammie, C. F., & Stone, J. M. 1999, ApJ, 513, 259
Ostriker, E. C., Stone, J. M., & Gammie, C. F. 2001, ApJ, 546, 980
Padoan, P., & Nordlund, A. P. 1999, ApJ, 526, 279
Sagdeev, R. Z., & Galeev, A. A. 1969, Nonlinear Plasma Theory (New York: Benjamin)
Saito, T., Kudoh, T., & Shibata, K. 2001, ApJ, 554, 1151
Solomon, P. M., Rivolo, A. R., Barrett, J., & Yahil, A. 1987, ApJ, 319, 730
Spitzer, L., Jr. 1942, ApJ, 95, 329
Schleuning, D. A. 1998, ApJ, 493, 811
Shu, F. H., Adams, F. C., & Lizano, S. 1987, ARA&A, 25, 23
Shu, F. H., Allen, A., Shang, H., Ostriker, E. C., & Li, Z.-Y. 1999, in The Origin of Stars and Planetary Systems, ed. C. J. Lada & N. Kylafis (Dordrecht: Kluwer), 193
Stone, J. M., & Norman, M. L. 1992, ApJS, 80, 791
Stone, J. M., Ostriker, E. C., & Gammie, C. F. 1998, ApJ, 508, L99
Tomisaka, K., Ikeuchi, S., & Nakamura, T. 1988, ApJ, 335, 239
Vrba, F. J., Strom, S. E., & Strom, K. M. 1976, AJ, 81, 958
Xiao, F., Yabe, T., & Ito, T. 1996, Comput. Phys. Commun., 93, 1
Xiao, F., Yabe, T., Peng, X., & Kobayashi, H. 2002, J. Geophys. Rev., 107 (D22), 4609
Yabe, T., & Aoki, T. 1991, Comput. Phys. Commun., 66, 219
Yabe, T., & Wang, P.-Y. 1991, J. Phys. Soc. Japan, 60, 2105
Yabe, T., Xiao, F., & Utsumi, T. 2001, J. Comput. Phys., 169, 556
Zuckerman, B., & Palmer, P. 1974, ARA&A, 12, 279
Zweibel, E. G., & Josafatsson, K. 1983, ApJ, 270, 511